Additive Manufacturing 23 (2018) 70–78

Contents lists available at ScienceDirect

Additive Manufacturing

journal homepage: www.elsevier.com/locate/addma

3D printed hierarchically-porous microlattice electrode materials for exceptionally high specific capacity and areal capacity lithium ion batteries

Mohammad Sadeq Saleh[a,1], Jie Li[b,1], Jonghyun Park[b,*], Rahul Panat[a,*]

[a] Department of Mechanical Engineering, Carnegie Mellon University, Pittsburgh, PA, 15213, USA
[b] Department of Mechanical and Aerospace Engineering, Missouri University of Science and Technology, Rolla, MO, 65409, USA

ARTICLE INFO

Keywords:
3D Printed batteries
Microlattice batteries
3D Microarchitected batteries
Ultrahigh capacity batteries
Aerosol jet printing

ABSTRACT

Despite the enormous potential of additive manufacturing in fabricating three-dimensional battery electrodes, the structures realized through this technology are mainly limited to the interdigitated geometries due to the nature of the manufacturing process. This work reports a major advance in 3D batteries, where highly complex and controlled 3D electrode architectures with a lattice structure and a hierarchical porosity are realized by 3D printing. Microlattice electrodes with porous solid truss members (Ag) are fabricated by Aerosol Jet 3D printing that leads to an unprecedented improvement in the battery performance such as 400% increase in specific capacity, 100% increase in areal capacity, and a high electrode volume utilization when compared to a thin solid Ag block electrode. Further, the microlattice electrodes retain their morphologies after 40 electrochemical cycles, demonstrating their mechanical robustness. These results indicate that the 3D microlattice structure with a hierarchical porosity enhances the electrolyte transport through the electrode volume, increases the available surface area for electrochemical reaction, and relieves the intercalation-induced stress; leading to an extremely robust high capacity battery system. Results presented in this work can lead to new avenues for improving the performance of a wide range of electrochemical energy storage systems.

1. Introduction

Advances in the electrochemical energy storage technologies such as Li-ion batteries have been realized not only by introducing new high energy/power materials, but also by creating new electrode architectures that increase surface area and mitigate mechanical instability [1,2]. Three dimensional (3D) porous electrode architectures with irregular or regular (e.g. lattice) geometries enhance the ingress of Li-ions into the host electrodes while reducing the total diffusion path, which can lead to an improved utilization of the electrode volume. Further, the facile transport of Li-ions leads to their uniform distribution along the electrodes, enhancing the tolerance of the battery to mechanical stress during demanding intercalation/de-intercalation cycles (similar to cellular materials such as bones [3]). In addition to energy storage, the 3D architected materials have been proposed as metamaterials, where mechanical, thermal and optical properties can be tuned by simple changes to their structures and shapes [4,5]. Although the potential benefits of such architectures are clear, a scalable and repeatable manufacturing process that can control porosity for a wide range of battery materials remains a significant challenge.

Several studies have been carried out that aim to fabricate electrodes with internal porosity and/or regular lattice structures [6–13]. Cathodes consisting of self-assembled nanolattices of an electrolytically active material sandwiched between rapid ion and electron transport pathways were shown to have high charge-discharge rates [13]. Si electrodes with porosity at a length scale of > 20 μm were shown to relieve strain and prevent pulverization of the anodes during electrochemical cycling [6]. Lattice electrodes made of carbon sprayed with Si particles [7] and sodium carboxymethyl cellulose [8] were used to improve the strain tolerance of batteries. Using a thermal annealing process, electrodes with a random arrangement of pores were obtained and showed an improved performance [9]. Freeze-casting was used to create directional porosity in graphene that led to fast electrochemical energy storage capabilities [14]. A pomegranate inspired battery architecture was developed with high capacity to tolerate lithiation strain [10]. Fundamental surface electrochemistry was studied for hollow gold tube electrodes with periodic pores fabricated by two-photon lithograph followed by atomic layer deposition and burnout of the polymer [15,16].

Although significant advances have been made in this area, the

* Corresponding authors.
E-mail addresses: parkjonghy@mst.edu (J. Park), rpanat@andrew.cmu.edu (R. Panat).
[1] These authors contributed equally to this work.

https://doi.org/10.1016/j.addma.2018.07.006
Received 9 April 2018; Received in revised form 10 July 2018; Accepted 11 July 2018
Available online 29 July 2018
2214-8604/

electrode shape control, especially in 3D, is rather limited either due to the nature of the templates or the etching processes used. Another limitation is the electrode material compatibility with chemicals used to create the porosity. Lastly, although the electrodes with special geometries such as hollow tubes [15,16] have controlled shapes; they offer a very limited amount of total electrode volume which is not practical for most applications. Some of the above issues could be addressed by fabricating 3D electrodes by slurries or particle dispersions using nozzle-based 3D printing techniques [17–19]. Paste extrusion was used to fabricate laminated interdigitated electrodes at length scales less than 1 mm [17]. Other interdigitated laminate electrodes for Li-ion batteries have also been realized by extrusion printing of graphene oxide [19] that resulted in a high mass loading. In our earlier work [18], high aspect ratio interdigitated structures were fabricated by extrusion-based additive manufacturing that overcame the tradeoff between high areal and high specific capacity. Recently, it was demonstrated that a simultaneous control of electrode shape (macrostructure) and microstructure could be used to enhance the battery performance [20]. These extrusion-based additive manufacturing methods, however, have three critical limitations. First, the interdigitated topology, although 3D, is only a subset of the possible spatial architectures. Second, the extrusion and inkjet printing has limited particle loading due to the viscosity effects [17]. Lastly, the interdigitated electrodes do not have a hierarchical structure, which may be needed for effective mechanical stress relief [21]. A rapid droplet-based printing of nanoparticle dispersions followed by sintering has the potential to overcome the limitations described above. For example, we have recently demonstrated that Aerosol Jet (AJ) 3D printing can be used to assemble nanoparticles in 3D space in the form of microscale networks with porous solid truss members [22].

This paper proposes a new innovative approach for fabricating complex 3D lattice battery electrodes with hierarchical porosity. The work aims to: (1) create a new fabrication approach for battery architectures that provides adequate degrees of freedom to ensure structural integrity and electrical connectivity, (2) enable a facile electrolyte immersion through open porosity to take full advantage of the energy storage capability of the active material, and (3) relax the stress by accommodating volume change during charge/discharge cycles. Toward this, AJ 3D printing is utilized to realize highly complex 3D microlattice electrodes with a hierarchical porosity over several orders of magnitude in length scale.

2. Materials and methods

2.1. Material preparation

A solvent-based Ag nanoparticle ink (Perfect-TPS 50 G2, Clariant Group, Frankfurt, Germany) was used to fabricate silver Li-ion battery electrodes primarily due to the commercial availability of the inks (i.e. dispersions) for this printing method [22,23]. In addition, it is known that silver exhibits a high specific capacity according to the formation of different Ag–Li alloys (up to $Li_{12}Ag$) in a very low voltage range versus lithium [24]. The Ag nanoparticle size in the ink was 30–50 nm, the ink viscosity was about 1.5 cP, and the Ag particle loading in the ink was about 40 ± 2 wt %.

2.2. Electrode fabrication

The electrodes were fabricated using AJ based 3D printing method [25]. A commercial AJ printer (AJ-300, Optomec, Inc., Albuquerque, NM) was used which allowed the deposition of nanoparticles dispersed in a solvent (i.e. the nanoparticle ink) onto a substrate by creating a mist of particles guided by a carrier gas. The AJ printing system included two atomizers (ultrasonic and pneumatic), a programmable XY motion stage, and a deposition head. The Ag nanoparticle ink was placed in the ultrasonic atomizer which continuously created a mist of droplets having sizes between 1–5 μm (each droplet containing multiple nanoparticles) which was then carried to the deposition head with a carrier N_2 gas [25,26]. The mist or dense vapor was then focused and driven toward the nozzle with the help of a sheath gas (also N_2) to form a micro-jet. Note that the pneumatic atomizer allows printing of thick inks with viscosities of up to 1000 cP but was not used in this work. The printing process was by a continues flow of droplets which was stopped or resumed by movement of a shutter. The particle agglomeration was prevented by placing the ink material in a tube which was rotated continuously around its axis for at least 12 h using a tube roller (Scilogex MX-T6-S, Rocky Hill, CT) prior to printing. The printhead nozzle had a diameter of 150 μm, which is known to give rise to an aerosol stream having diameter of ~10–15 μm [23]. Before printing, the geometry of the conductive part was drawn in AutoCAD using a program in the software AutoLISP (AutoCAD 2015, Autodesk Inc., San Rafael, CA) and converted to a "prg" file compatible with the printer software. The flow rate in the AJ machine during printing was 25 sccm, while that for the sheath gas was 50 sccm. The printed pattern was thermally sintered in a programmable oven (Neytech Vulcan furnace, Model 3–550, Degussa-Ney Dental Inc., Bloomfield, CT) at 350 °C for 2 h. Stainless steel connector disks with 11 mm diameter and 500 μm thickness were coated with 50 nm chromium and used as substrates for the printed electrodes.

2.3. Electrode characterization and battery assembly

The morphologies of the printed and sintered 3D electrodes were characterized using Scanning Electron Microscopy (SEM, Hitachi S4700, Hitachi Ltd., Japan). A Focused Ion Beam (FIB, FEI Corp., Hillsboro OR) cut was used to obverse porosity within the truss members of the microlattice. The battery was assembled in a CR2032 coin cell (Wellcos Corp, Korea) in an argon-filled glove box (Mbraun). The printed silver microlattices were used as anodes, Li foil was used as the cathode, and a commercial PP/PE/PP membrane (Celgard) was used as the separator. The battery was filled with liquid electrolyte 1 M $LiFP_6$ EC:PC:EMC 1:1:3 (Sigma-Aldrich).

2.4. Electrochemical measurements

The electrochemical behavior of the assembled batteries was measured from 0.02 to 2.8 V by using a battery testing station (IVIUMnSTAT, Ivium Tech, The Netherlands). The battery capacity was measured under different C-rates, which were calculated based on mass of silver and experimental theoretical specific capacity (290 mA h/g) [27]; while the battery impedance was measured using electrochemical impedance spectroscopy (EIS) at 0.2 V open circle voltage. Silver electrode samples in the shapes of solid blocks and 3D lattice structures having the same foot area but different thicknesses of 250 and 450 μm were tested in this study.

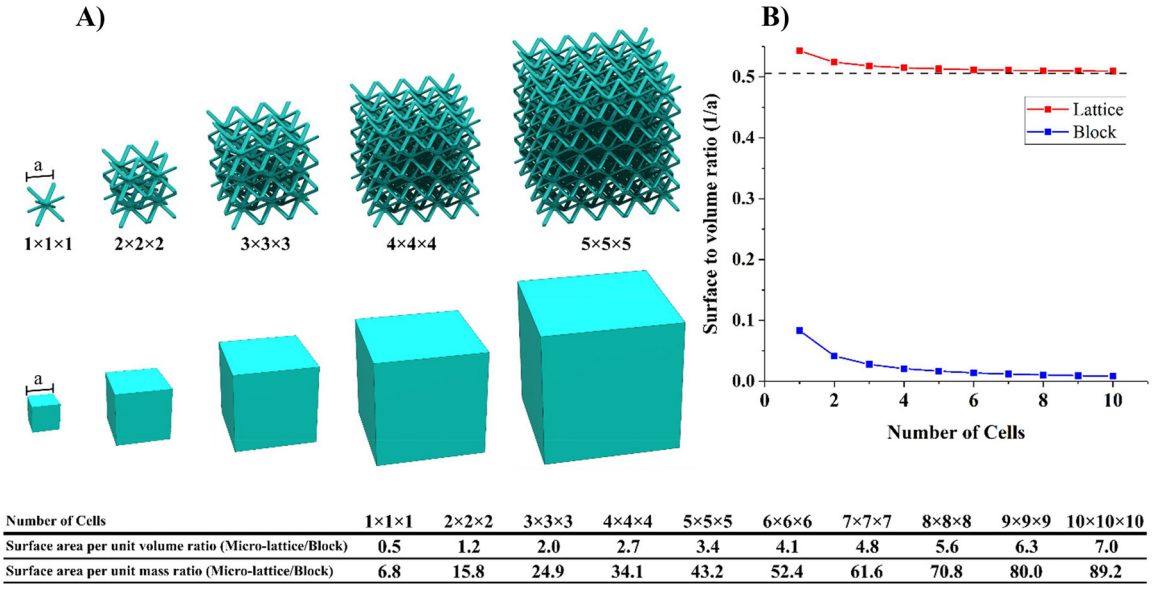

Number of Cells	1×1×1	2×2×2	3×3×3	4×4×4	5×5×5	6×6×6	7×7×7	8×8×8	9×9×9	10×10×10
Surface area per unit volume ratio (Micro-lattice/Block)	0.5	1.2	2.0	2.7	3.4	4.1	4.8	5.6	6.3	7.0
Surface area per unit mass ratio (Micro-lattice/Block)	6.8	15.8	24.9	34.1	43.2	52.4	61.6	70.8	80.0	89.2

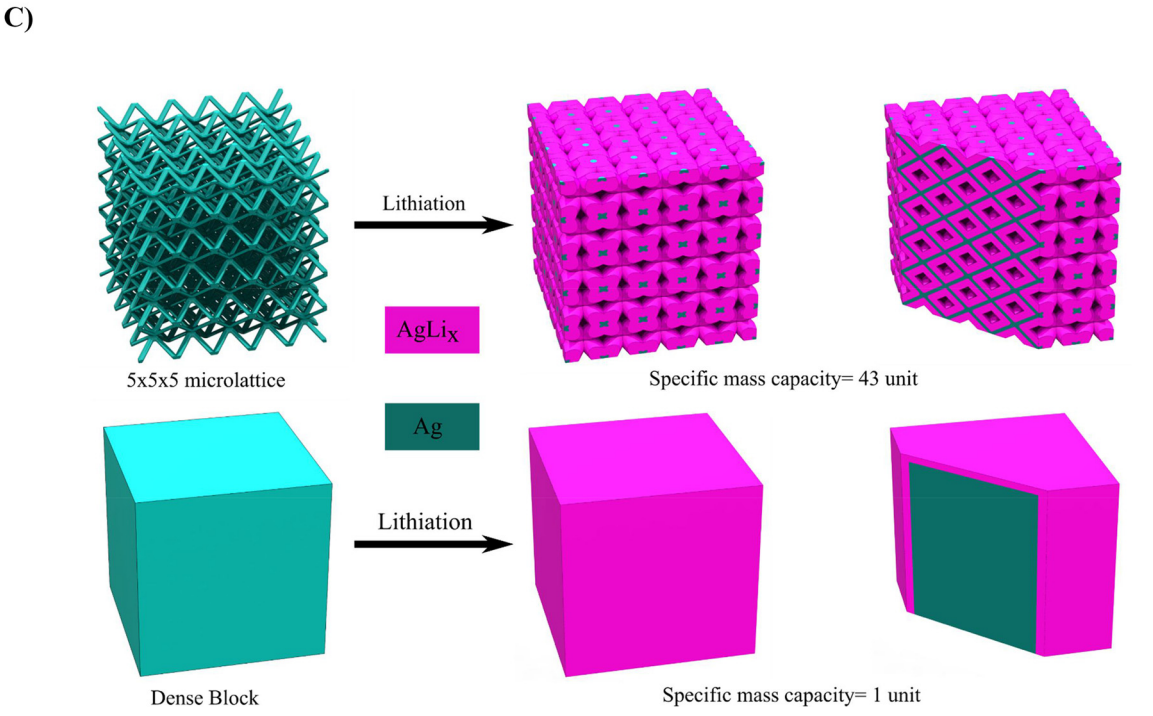

Fig. 1. (A) Body centered cubic lattice is compared with simple dense cube of same overall size. The length to diameter ratio of each truss of the lattice is about 10 in this example. (B) A comparison of surface area to volume ratio as the number of cells increases. The lattice surface to volume ratio asymptotically converge to 0.50 while the cube converges to zero. The y axis in the graph is normalized by dividing the S/V ratio by single cell edge length (a). (C) Lattice architecture can provide channels for effective transportation of electrolyte inside the volume of material, while for the cube electrode, most of the material will not be exposed to the electrolyte. The cross-section view shows the silver mesh enabling the charge (Li^+ ions) transportation to the current collector and how most of the printed material has been utilized.

3. Results and discussion

3.1. Microlattice design and architecture

A 3D microlattice architecture having a unit cell with an open octahedral structure is selected to demonstrate the proposed technology (Fig. 1A). Note that the unit cell determines the porosity and surface-to-volume ratio of the cell, which in-turn controls the battery electrochemical and mechanical properties. In particular, the degree of freedom at the joints of the unit cell determines the mechanical strain

tolerance of the structure. In the open octahedral microlattice geometry shown in Fig. 1(A), each link is connected to three nearest and four other links at each end, while a given joint holds eight links together, which reduces the risk of an electronic disconnection due to stresses during the charge/discharge cycles. The special geometric feature that makes this lattice ideal for batteries is its 'open foam' architecture that ensures free transport for electrolyte and hence the uniform diffusion of the host ions at the electrode surface (e.g. Li^+ in the case of Li-ion batteries) regardless of the link thicknesses and the overall sample volume. In addition, the unit cell in the lattice is not fully mechanically constrained, allowing considerable electrode deformation. This can be estimated by Maxwell's criterion, $M = -3j + b + 6$, where M represents the number of modes, j represents the number of frictionless joints (6 for the structure in Fig. 1A), and b is the number of links (8 for the structure in Fig. 1A) [28]. Accordingly, four soft modes of deformation can be expected in the proposed structure. With high numbers of soft modes for the lattice, the proposed structure can have a high strain tolerance which mitigates the electrochemical stress when swelling occurs under charge/discharge cycles, and when compressive loads arise from the cell boundaries (such as casing).

To elaborate on the effect of electrode material architecture on the increase in the surface area, the lattice geometry is compared with an equivalent thin block of active material (Fig. 1A, B). A high surface area to volume (S/V) ratio can provide an enhanced transport for the intercalation process and allow better material utilization. For a cube, the S/V ratio is inversely proportional to its edge length and becomes smaller as the cube size increases. However, the S/V ratio for a lattice structure remains constant as the number of cells (i.e., overall size) increases and is much higher (up to 3.4 times more for $5 \times 5 \times 5$) than the cubes (Fig. 1B). Another aspect of battery technology is the battery areal capacity. One way to increase the areal capacity is to add more material by increasing the thickness of the electrodes. This approach, however, limits the transport of ions and electrons, resulting in poor power performance and inefficient utilization of materials. The proposed 3D lattice structure can address this issue. Although micro-architectures have less active material than solid blocks; they can result in effective utilization of the electrode volume, and can increase specific capacity and areal capacity. Further, with the proposed technology, the porosity within the truss members of the microlattice can be adjusted so that hierarchical porosity can be achieved for effective stress relief. The schematic in Fig. 1(C) shows the lithiation for a $5 \times 5 \times 5$ lattice and a dense block of equivalent overall size. The charge carrying capacity of the lattice electrodes is significantly higher than that for the block electrode for the same amount of charging time.

3.2. Fabrication of three-dimensional microlattice electrodes

Fig. 2(A) shows the schematic of the printing process to form the complex microlattice electrodes. Droplets containing silver nanoparticles exit from the AJ nozzle with a diameter of about 1–5 μm [25] and a particle loading of about 70% [22]. Several of the droplets coalesce and form a mass of nanoparticles that reaches the substrate. The platen on which the printing occurs was heated to 110 °C, which helped dry the mass of nanoparticles (diameter of about 20 μm in the present case) by removing the solvents within about 1s [22]. The next set of droplets were then dispensed at an offset as shown in Fig. 2(A). In order for these to adhere to the previously formed pillar, we use the fact that the surface forces of the droplets scale as r^2, while the inertia forces scale as r^3, where r is the radius of the droplet. This allowed strong adhesion forces for the droplet as compared to its inertia forces (i.e. weight) at length scales of 100 μm or less [29]. As a result of this scaling, the printed droplet adhered to the pillar rather than falling off from it. The platen heat then removed the solvent such that the pillar is ready to receive the next droplet containing silver nanoparticles. This process was continued until a full lattice was formed. The printing process described here is very rapid as will be discussed later. The minimum angle θ in Fig. 1(A) for a flat ledge has been calculated to be approximately 30-40° depending upon the droplet properties [22]. Sintering at 350 °C for 2 h, is expected to remove the binders and sinter the nanoparticles to form metallic truss members of the microlattice with internal porosity.

Fig. 2(B) shows schematics of the printing and sintering processes for the entire microlattice electrode. The printed 3D electrode is shown in Fig. 2(C), where the complex lattice geometry along with the porosity at different length scales are clearly observed. The printing produced controlled porosity at approximately 100–300 μm length scale (left image of Fig. 2A and C). The smaller porosity, on the other hand, is at 1 μm length scale and obtained from sintering the 3D lattice to a temperature of 350 °C (FIB section shown in the right image of Fig. 2C). The percentage of smaller porosity can be controlled from 1% to 20% for Ag by varying the sintering temperature [30]. The entire hierarchical porous electrode structure shown in Fig. 2(C), to the best of our knowledge, is the first report.

Table 1 shows the weight and dimension of the microlattice and solid electrodes fabricated by the AJ method. Fig. 3(A, B) show lattice electrodes (top and side images) with heights of about 450 μm and 250 μm at different magnifications, respectively. Fig. 3(C) shows a solid block of Ag with the similar overall dimension as the sample in Fig. 3(A) printed using the AJ method and used for comparison. A similar electrode with the same dimensions as Fig. 3(B) was also printed in the solid-block form and used for comparison (not shown). The higher magnification image of the solid block shows surface texture of the order of 100 nm to 500 nm. It is clear from the images in Figs. 2(C) and 3 that the AJ printing method can create highly controlled microlattice structures made of sintered nanoparticles with hierarchical porosities ranging from 100 s μm to a few microns or less within the structure.

3.3. Electrochemical performance

Fig. 4 shows the comparison of the electrochemical performance of the lattice samples (A1 and B1) and block samples (C1 and D1) in terms of specific capacity (Fig. 4A) and areal capacity (Fig. 4B). As shown in Fig. 4(A), the lattice samples have significantly improved specific capacity, which is up to four times that of the block samples, and close to the highest reported value for Ag in the literature (290 mA h/g) [27]. Note that our samples are much thicker than that in Ref. [27]. For areal capacity shown Fig. 4(B), we observe that the lattice sample (A1) has achieved an areal capacity of 5 mA h/cm^2 in the first cycle, which is twice that of the block sample. Comparing samples with the same structure (A1 versus B1 or C1 versus D1) in Fig. 4(B), it can be seen that thinner electrodes have a better areal capacity at least during the initial cycles (see further discussion later in this section). It is clear from Fig. 4 that lattice structures at both the thicknesses could significantly improve the areal capacity and specific capacity. In conclusion, this result indicates that the lattice electrodes had a high utilization of the active

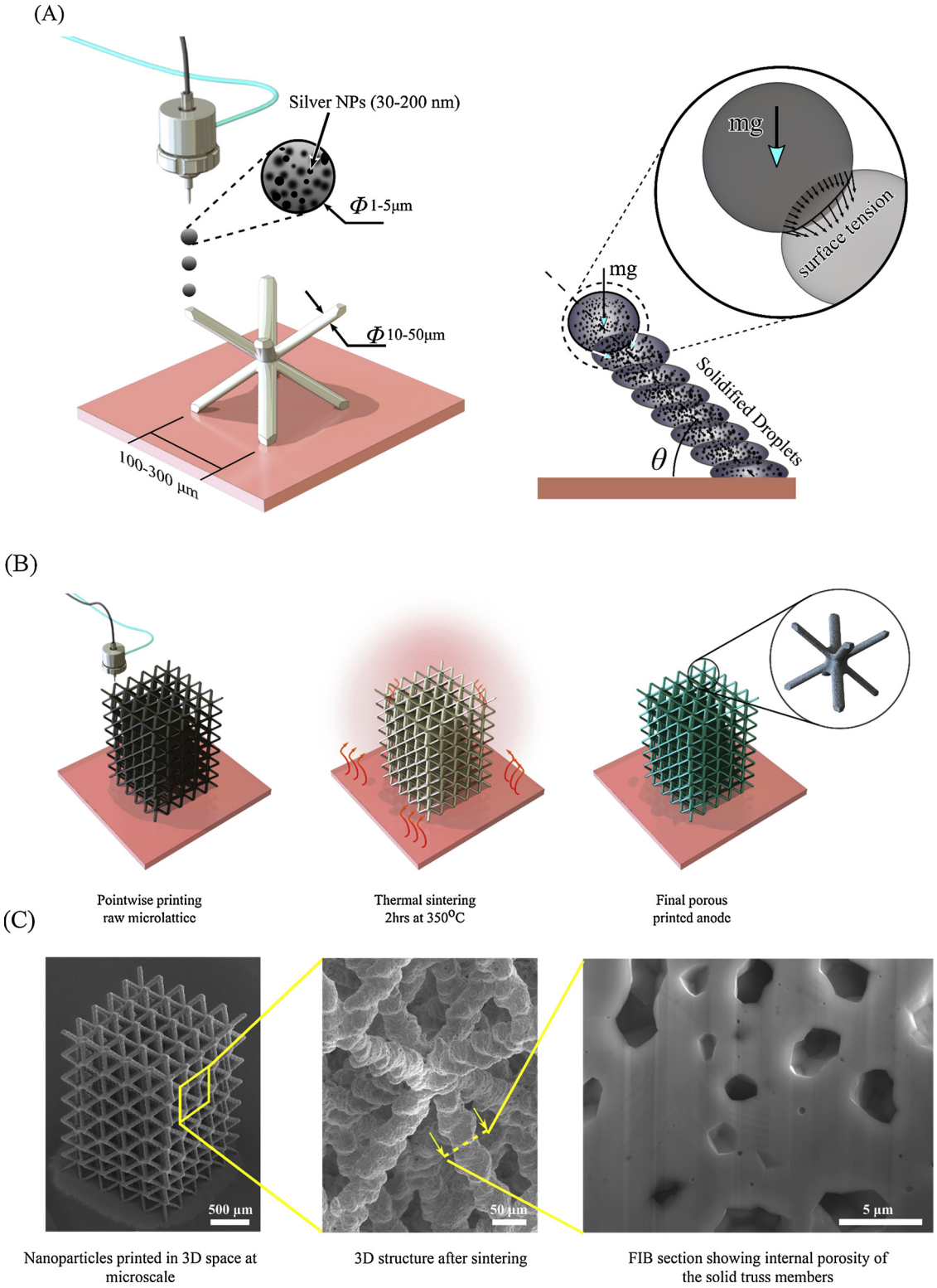

Fig. 2. (A) Schematic of the fabrication of 3D micro-architected battery electrodes by assembling nanoparticles in 3D space at microscale using the aerosol jet printing process. Heat removes the binders and sinters the nanoparticles to form the 3D microlattice with hierarchical porosity. (B) Schematic of the formation of 3D microlattice. (C) Representative SEM images of the 3D microlattice fabricated by the process described in (A) and (B). The FIB image shows a representative section of the truss member of the microlattice. Porosity at a length scale of 100 microns or more is seen from printing; while porosity at a length scale of about a micron is seen within the truss members.

Table 1
Physical parameters of the 3D lattice electrode structures.

Sample #	Structure	Mass (g)	Height (μm)
A1	Microlattice	0.0008211	215
A2	Microlattice	0.0018789	265
B1	Microlattice	0.000709	415
B2	Microlattice	0.002101	473
C1	Block	0.01458	457
C2	Block	0.0107871	460
D1	Block	0.003605	254
D2	Block	0.0036048	266

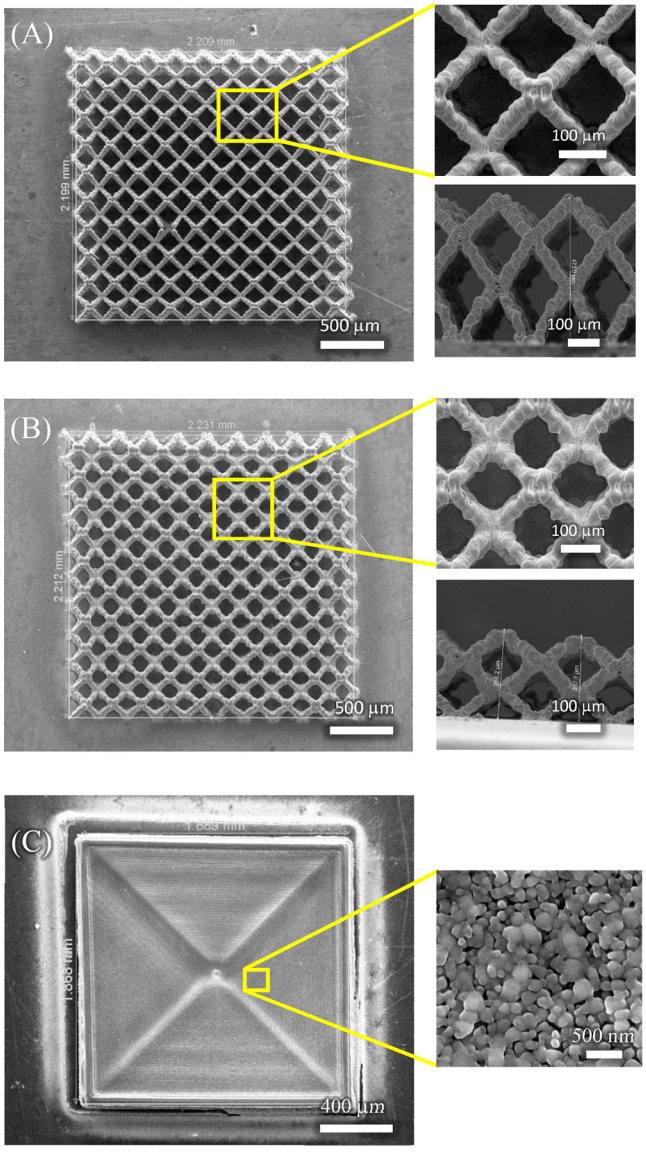

Fig. 3. SEM Images of 3D printed electrodes for Li-ion batteries used for electrochemical cycling in this study. (A, B) Top and side images of microlattice electrodes with heights of about 250 μm and 450 μm, respectively. (C) Solid block of Ag with same dimension as the microlattice printed using the AJ method.

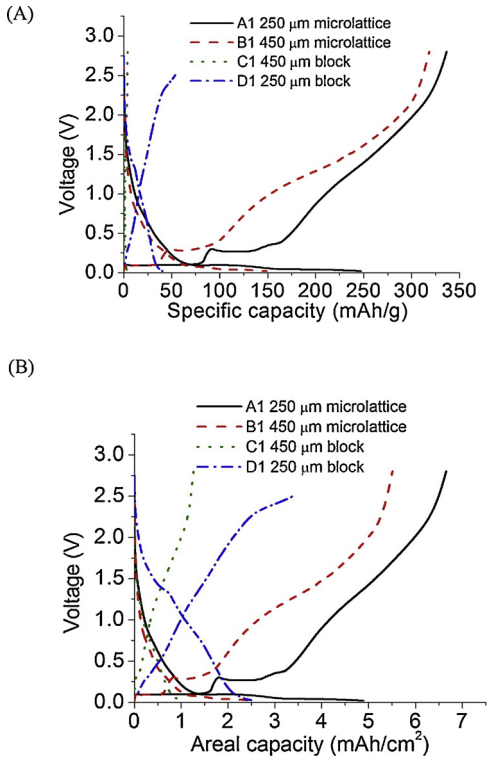

Fig. 4. (A) Specific capacity and (B) areal capacity for the microlattice and block structures, each with thicknesses of about 250 μm and 450 μm.

material (specific capacity is close to the highest reported values) with much thicker electrodes, indicating a higher areal capacity than the reported values [27]. The corresponding power density is about 22 μW/mm^2.

In order to study their cycle and rate performance, each cell was cycled at different C-rates of 0.1C, 0.2C, 0.5C, and 1C, and then again with 0.1C as shown in Fig. 5(A). A total of 40 cycles were applied to the batteries. The first five to seven cycles in Fig. 5(A) at 0.1C can be considered as 'formation cycles'. During formation cycles, the specific capacity of the batteries can increase likely because of progressively improved wetting of the electrode by the electrolyte until an equilibrium is reached. As expected, the performance became stable beyond these initial cycles at the given C-rate.

The lattice samples (A1 and B1) exhibited significantly higher specific capacity at every C-rate when compared to the block samples (C1 and D1). After cycling, the lattice samples (A1 and B1) also showed a good stabilized specific capacity of about 210 mA h/g owing to the 3D structure which facilitates electrolyte transport through the electrode volume. On the other hand, the block samples (C1 and D1) showed poor specific capacity likely resulting from the poor utilization of the active materials in that structure. In particular, D1 represented a stabilized specific capacity of about 95 mA h/g, and C1 exhibited poor performance of 22 mA h/g. The specific capacity of the samples A2, B2, C2, and D2 (Table 1) as a function of electrochemical cycling followed a trend similar to that shown in Fig. 5A (see Fig. S1 of supporting information). Fig. 5(B) compares the average specific capacity for the electrode structures after the formation cycles. Despite some variation depending upon samples, which might be caused by different material

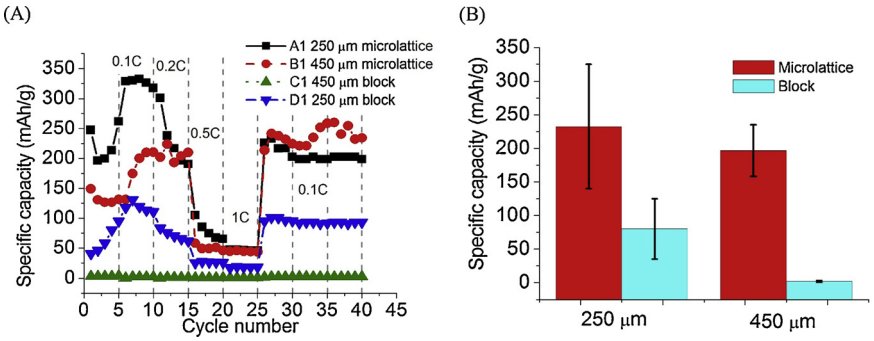

Fig. 5. (A) Specific capacity of the microlattice and block electrodes as a function of number of cycles at different C-rates. (B) Comparison of the average specific capacity of microlattice and block structure thicknesses of 250 μm and 450 μm.

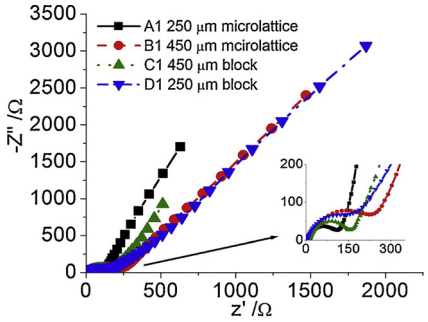

Fig. 6. Impedance for the microlattice (A1 and B1) and solid block (C1 and D1) electrodes.

batches, it can be confirmed that the microlattice electrode structures significantly enhance the battery performance when compared to the block electrode structures.

We note that in case of the block electrodes, the thick electrodes showed a considerable reduction in capacity (80% loss) compared to the thin electrodes, likely due to lower electrode utilization at a given time. The specific capacity of the thick 3D lattice electrode was slightly reduced by about 10% in the initial cycles. Beyond about 10 cycles, thought, the specific capacity of the thicker lattice sample is comparable or even slightly higher than the thinner lattice sample. It is note that adding more material by increasing the thickness of electrodes is a common method to increase the mass loading of the electrode; but it limits the transport of ions and electrons resulting in poor power performance and inefficient utilization of electrode material near the electrode-current collector interface. The 3D structure is expected to facilitate a facile transport of ions via a shorter diffusion path with an enhanced electrochemical reaction through a larger interface area. The data in Fig. 5(A) confirms this hypothesis and shows that the microlattice structure is able to maintain the specific capacity and hence scale the total capacity with increasing thickness of the electrodes.

An electrochemical impedance spectroscopy test was conducted on the microlattice and block samples to further understand the effect of lattice structure on the battery performance. The Nyquist plots for the four samples (A1, B1, C1, and D1) are shown in Fig. 6. The original data was fitted by a circuit diagram model of $R_e(C_{sl}R_{sl})(C_{dl}R_{ct}Z_w)$. The high-frequency intercept at the Z' axis corresponds to the ohmic resistance, R_e, which represents the resistance of the electrolyte, and the semicircle in the middle-frequency range indicates the charge transfer resistance, R_{ct}. The Warburg impedance, Z_w, which is related to a combined effect of the diffusion of lithium ions on the electrode/electrolyte interfaces, corresponds to the straight sloping line at the low-frequency end. It can be seen that both cells had a similar (10 ~ 20 Ω) ohmic resistance, but the semicircle of the A1 lattice structure was smaller than that of other structures. From the fitted impedance parameters, the charge transfer resistance, R_{ct}, of the A1 lattice structure ($R_{ct} \approx$ 86 Ω) indicates that inserting and de-inserting lithium ions from lattice structures was easier than that from the other structures. This result shows that the lattice electrode enhanced the transport of lithium ions, in confirmation of the results discussed in Figs. 4 and 5.

3.4. Mechanical integrity

Silver materials are limited in their use as battery active materials due to their large volumetric expansion during lithium insertion [31]. To better understand the effect of the 3D lattice structure on electrode volumetric expansion, we imaged the 250 μm thick 3D lattice electrode using SEM in as-fabricated, lithiated, and fully de-lithiated conditions after 40 cycles as shown in Fig. 7(A–C). It can be observed that after intercalation with Li-ions, the structures are changed considerably but retained the overall shape. This is interesting given the fact that the lattice network is reported to have high stress localization and fracture around the nodes when loaded in compression [32]. Although we did not observe failure at the lattice nodes in this work (where the loading is internal expansion/contraction), optimization strategies for reducing local stress at nodes can be employed to mitigate this potential issue. Further, suitable nanolaminates [33] can be deposited over the 3D architectures developed in this work using methods such as atomic layer deposition (ALD) to increase the nodal strength. To assess the specific changes to morphology, the as-fabricated and de-lithiated electrodes were observed under SEM at higher magnifications as shown in Fig. 7(D–G), respectively. On average, the individual truss members increased in diameter by about 15–20% after the Li intercalation/de-intercalation cycles. Further, the lithiation cycle gave the electrode a 'corrosion' like surface texture along with several cracks; a likely effect of the electrochemical process and volumetric changes to the electrode. Note that during the cycling process, the pores inside the lattice are likely occupied with $AgLi_x$. In case of the block structure, the overall area was observed to increase by about 11% for each of the planar directions. For the thicker samples (B1 and C1), cracks were generated over the samples and the electrodes were broken during disassembly, preventing an observation of the electrode post assembly in that case.

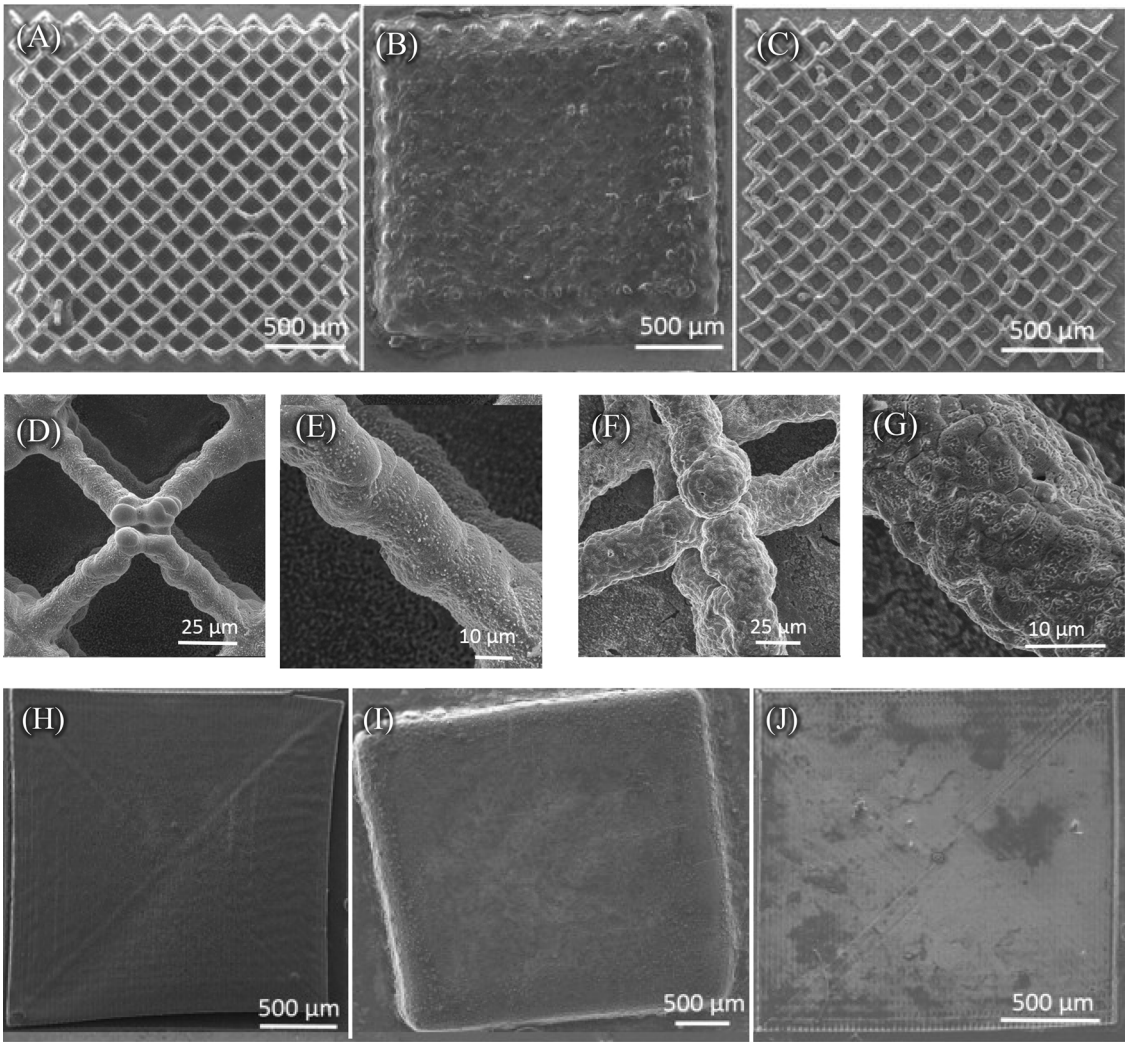

Fig. 7. SEM of 250 µm thick silver microlattice electrode structure. (A) as fabricated, (B) fully lithiated, and (C) fully de-lithiated. (D, E) Higher magnification images of the as-fabricated electrode in (A). (F, G). Higher magnification imaged of the fully de-lithiated electrode in (C). (H–J) SEM images of the 250 µm thick block electrode in as fabricated, fully lithiated, and fully de-lithiated conditions, respectively.

The additive manufacturing method presented in this work is a major advance in the realization of complex geometries for 3D battery architectures. The work is also an important step toward the realization of geometrically optimized 3D configurations for electrochemical energy storage. The experimental results show that batteries with hierarchical porosity can be fabricated by the nanoparticle-based additive printing method. For example, the time taken to fabricate the electrode shown in Fig. 2(B) is about 40 min for 1 printhead. The equipment technology for AJ has advanced to 4 printheads working in tandem. The printing can potentially be extended to the inkjet process, where existing systems have thousands of printheads working in tandem, which will further scale up the fabrication of such electrodes. The results clearly show a strong advantage of the lattice batteries with hierarchical porosity in terms of the volumetric and areal capacity, electrode volume utilization, and mechanical robustness of the system.

4. Conclusions

In this study, we propose and demonstrate a 3D printing method that leads to the fabrication of highly complex microlattice electrode architectures for high capacity robust Li-ion batteries. The microlattice electrodes are tested to demonstrate a significantly improved battery performance when compared to solid block electrodes. The electrode fabrication process involves the direct printing of droplets of nanoparticle dispersions followed by heating to remove the solvents and sinter the nanoparticles. We show that the printing process creates 3D feature sizes of the order of 100 µm, with solid metallic truss members having diameters of ~20-50 µm. Further, the sintering process creates porosity within the truss members at a length scale of about a micron, thus forming a hierarchical porous system with a very high surface to volume ratio for the structure. The specific charge capacity and areal capacity of the 3D microlattice electrodes are shown to be several times that for comparable solid block electrodes, indicating the effectiveness of electrolyte penetration in the porous structure and improved utilization of electrode active material during the lithiation/de-lithiation cycles. The 3D architectures also show a strain tolerance to deformation as they retain the shape during multiple lithiation and delithiation cycles in spite of size changes of the order of 20% for the truss members

within the microlattice structure. These results represent a significant advance in the realization of complex optimized 3D geometries/topologies for electrodes in Li-ion batteries and other electrochemical energy storage systems.

Author contributions

R.P., J.P., M.S.S., and J.L. designed the research. J.L. and M.S.S. performed the experiments. R.P., J.P., M.S.S., and J.L. analyzed the data. R.P., J.P., M.S.S., and J.L. wrote the manuscript. M.S.S., and J.L. contributed equally to this work.

Competing interests

The authors declare no competing financial interests.

Acknowledgements

This material is based upon work supported by the National Science Foundation under Grant Nos. CMMI-1747608 and CMMI-1563029. Part of the microscopy work was performed at the Nanoscience Fabrication and Characterization Facility at the University of Pittsburgh, under CMU-Pittsburgh collaborative agreement and the Franceschi Center at the Washington State University, Pullman WA. Part of the microscopy work was performed at the Material Research Center at Missouri University of Science and Technology with Junior Faculty Support.

Appendix A. Supplementary data

Supplementary material related to this article can be found, in the online version, at doi:https://doi.org/10.1016/j.addma.2018.07.006.

References

[1] M. Yoshio, R.J. Brodd, A. Kozawa, Lithium-Ion Batteries, Springer, 2009.
[2] J.W. Long, B. Dunn, D.R. Rolison, H.S. White, Three-dimensional battery architectures, Chem. Rev. 104 (10) (2004) 4463–4492.
[3] L.J. Gibson, M.F. Ashby, B.A. Harley, Cellular Materials in Nature and Medicine, Cambridge University Press, 2010.
[4] Y. Chen, T. Li, F. Scarpa, L. Wang, Lattice metamaterials with mechanically tunable Poisson's ratio for vibration control, Phys. Rev. Appl. 7 (2) (2017) 024012.
[5] X. Li, H. Gao, Mechanical metamaterials: smaller and stronger, Nat. Mater. 15 (2016) 373.
[6] X. Li, M. Gu, S. Hu, R. Kennard, P. Yan, X. Chen, C. Wang, M.J. Sailor, J.-G. Zhang, J. Liu, Mesoporous silicon sponge as an anti-pulverization structure for high-performance lithium-ion battery anodes, Nat. Commun. 5 (2014).
[7] J. Guo, X. Chen, C. Wang, Carbon scaffold structured silicon anodes for lithium-ion batteries, J. Mater. Chem. 20 (24) (2010) 5035–5040.
[8] J. Guo, C. Wang, A polymer scaffold binder structure for high capacity silicon anode of lithium-ion battery, Chem. Commun. 46 (9) (2010) 1428–1430.
[9] H. Kim, B. Han, J. Choo, J. Cho, Three-dimensional porous silicon particles for use in high-performance lithium secondary batteries, Angew. Chem. 120 (52) (2008) 10305–10308.
[10] N. Liu, Z. Lu, J. Zhao, M.T. McDowell, H.-W. Lee, W. Zhao, Y. Cui, A pomegranate-inspired nanoscale design for large-volume-change lithium battery anodes, Nat. Nanotechnol. 9 (3) (2014) 187–192.
[11] Y. Zhao, X. Liu, H. Li, T. Zhai, H. Zhou, Hierarchical micro/nano porous silicon Li-ion battery anodes, Chem. Commun. 48 (42) (2012) 5079–5081.
[12] A. Esmanski, G.A. Ozin, Silicon inverse-opal-based macroporous materials as negative electrodes for lithium ion batteries, Adv. Funct. Mater. 19 (12) (2009) 1999–2010.
[13] J.H. Pikul, H.G. Zhang, J. Cho, P.V. Braun, W.P. King, High-power lithium ion microbatteries from interdigitated three-dimensional bicontinuous nanoporous electrodes, Nat. Commun. 4 (2013) 1732.
[14] Y. Shao, M.F. El-Kady, C.W. Lin, G. Zhu, K.L. Marsh, J.Y. Hwang, Q. Zhang, Y. Li, H. Wang, R.B. Kaner, 3D freeze-casting of cellular graphene films for ultra-high-power-density supercapacitors, Adv. Mater. 28 (31) (2016) 6719–6726.
[15] C. Xu, B.M. Gallant, P.U. Wunderlich, T. Lohmann, J.R. Greer, Three-dimensional Au microlattices as positive electrodes for Li–O2 batteries, ACS Nano 9 (6) (2015) 5876–5883.
[16] T.A. Schaedler, A.J. Jacobsen, A. Torrents, A.E. Sorensen, J. Lian, J.R. Greer, L. Valdevit, W.B. Carter, Ultralight metallic microlattices, Science 334 (6058) (2011) 962–965.
[17] K. Sun, T.S. Wei, B.Y. Ahn, J.Y. Seo, S.J. Dillon, J.A. Lewis, 3D printing of interdigitated Li-Ion microbattery architectures, Adv. Mater. 25 (33) (2013) 4539–4543.
[18] J. Li, M.C. Leu, R. Panat, J. Park, A hybrid three-dimensionally structured electrode for lithium-ion batteries via 3D printing, Mater. Des. 119 (2017) 417–424.
[19] C.C. Ho, K. Murata, D.A. Steingart, J.W. Evans, P.K. Wright, A super ink jet printed zinc–silver 3D microbattery, J. Micromech. Microeng. 19 (9) (2009) 094013.
[20] J. Li, X. Liang, F. Liou, J. Park, Macro-/micro-controlled 3D lithium-ion batteries via additive manufacturing and electric field processing, Sci. Rep. 8 (1) (2018) 1846.
[21] T. Lan, Y. Liu, J. Dou, Z. Hong, M. Wei, Hierarchically porous TiO 2 microspheres as a high performance anode for lithium-ion batteries, J. Mater. Chem. A 2 (4) (2014) 1102–1106.
[22] M.S. Saleh, C. Hu, R. Panat, Three-dimensional microarchitected materials and devices using nanoparticle assembly by pointwise spatial printing, Sci. Adv. 3 (3) (2017).
[23] M.T. Rahman, J. McCloy, C. Ramana, R. Panat, Structure, electrical characteristics, and high-temperature stability of aerosol jet printed silver nanoparticle films, J. Appl. Phys. 120 (7) (2016) 075305.
[24] G. Taillades, J. Sarradin, Silver: high performance anode for thin film lithium ion batteries, J. Power Sources 125 (2) (2004) 199–205.
[25] J.A. Paulsen, M. Renn, K. Christenson, R. Plourde, Printing conformal electronics on 3D structures with aerosol jet technology, Future of Instrumentation International Workshop (FIIW), 2012, IEEE, (2012), pp. 1–4.
[26] M.J. Renn, M. Essien, B.H. King, J.A. Paulsen, Aerodynamic jetting of aerosolized fluids for fabrication of passive structures, USPTO, Optomec Design Company, US, #7674671 B2, 2010.
[27] H.-R. Jung, W.-J. Lee, Ag/poly (3, 4-ethylenedioxythiophene) nanocomposites as anode materials for lithium ion battery, Solid State Ionics 187 (1) (2011) 50–57.
[28] M. Ashby, The properties of foams and lattices, philosophical transactions of the royal society of London a: mathematical, Phys. Eng. Sci. 364 (1838) (2006) 15–30.
[29] G.K. Batchelor, An Introduction to Fluid Dynamics, Cambridge University Press, 2000.
[30] M. Sadeq Saleh, M. HamidVishkasougheh, H. Zbib, R. Panat, Polycrystalline micropillars by a novel 3-D printing method and their behavior under compressive loads, Scr. Mater. 149 (2018) 144–149.
[31] L. Fu, K. Tang, C.-C. Chen, L. Liu, X. Guo, Y. Yu, J. Maier, Free-standing Ag/C coaxial hybrid electrodes as anodes for Li-ion batteries, Nanoscale 5 (23) (2013) 11568–11571.
[32] Y. Chen, T. Li, Z. Jia, F. Scarpa, C.-W. Yao, L. Wang, 3D printed hierarchical honeycombs with shape integrity under large compressive deformations, Mater. Des. 137 (2018) 226–234.
[33] J. Wang, Q. Zhou, S. Shao, A. Misra, Strength and plasticity of nanolaminated materials, Mater. Res. Lett. 5 (1) (2017) 1–19.